



HAL
open science

Prediction of linear and non-linear behavior of 3D woven composite using mesoscopic voxel models reconstructed from X-ray micro-tomography

Yang Liu, Ilya Straumit, Dmytro Vasiukov, Stepan V. Lomov, Stéphane Panier

► To cite this version:

Yang Liu, Ilya Straumit, Dmytro Vasiukov, Stepan V. Lomov, Stéphane Panier. Prediction of linear and non-linear behavior of 3D woven composite using mesoscopic voxel models reconstructed from X-ray micro-tomography. *Composite Structures*, 2017, 179, pp.568 - 579. 10.1016/j.compstruct.2017.07.066 . hal-01882925

HAL Id: hal-01882925

<https://hal.science/hal-01882925>

Submitted on 24 Nov 2023

HAL is a multi-disciplinary open access archive for the deposit and dissemination of scientific research documents, whether they are published or not. The documents may come from teaching and research institutions in France or abroad, or from public or private research centers.

L'archive ouverte pluridisciplinaire **HAL**, est destinée au dépôt et à la diffusion de documents scientifiques de niveau recherche, publiés ou non, émanant des établissements d'enseignement et de recherche français ou étrangers, des laboratoires publics ou privés.

Prediction of linear and nonlinear behavior of 3D woven composite using mesoscopic voxel models reconstructed from X-ray micro-tomographyYang Liu ^a, Ilya Straumit ^b, Dmytro Vasiukov ^{a,*}, Stepan V. Lomov ^b, Stéphane Panier ^{a,c}^a Polymers and Composites Technology & Mechanical Engineering Department, IMT Lille Douai, France^b Department of Materials Engineering (MTM), KU Leuven, Belgium^c Laboratoire des Technologies Innovantes, LTI-EA 3899, Université de Picardie Jules Verne, Amiens, 80025 France**Abstract**

Mesoscopic representative volume cells (RVCs), reflecting the internal structure of a 3-Dimensional (3D) orthogonal weave composite were reconstructed in this work from X-ray micro-tomography (μ CT) images. Compared with the conventional idealized modelling strategy, voxel models are able to reproduce the varied yarn cross-section and the non-fully-symmetric undulated yarn path. Local details of the yarn geometry seem to influence only slightly the prediction of the elastic properties but are shown to influence significantly the damage and failure performance. Continuum damage models are formulated and implemented in the user subroutine UMAT of ABAQUS/Standard. The strength predicted with the model generated from the μ CT images shows a better agreement with the experimental results compared to an idealized model. Damage is calculated along the loading history. The statistic distribution of damage variable is employed to describe the overall damage intensity when the peak stress value is reached. The quantitative analysis shows that the reproduced unevenness and the pre-defects of the yarns are prone to incurring damage and to confining the damage inside the RVC.

Keywords: 3-Dimensional reinforcement, Modelling strategy, X-ray micro-tomography (μ CT), Progressive damage analysis (PDA),

1. Introduction

3D woven composites have a wide potential in a range of industries such as aerospace, automobile, marine, civil engineering etc., as Mouritz was discussed nearly two decades ago [1]. If it is required the multi-directional load bearing capacity, higher delamination resistance, and better anti-impact performance the 3D textile reinforced composites are becoming competitive with the conventional 2D laminated composites.

Progressive failure analysis has been broadly employed to investigate the damage and failure behavior of 3D textile composites in on-axis tension [2–6], off-axis tension [6–8], compression [9,10], flexure [4,11] and impact [12]. The 3D failure criteria, which usually define the damage initiation surface inside the effective stress space, such as Hashin's [2,7,8,13], Hoffman's [14,15], Pinho's [3] and Puck's [4] criteria have manifested excellent capacity to detect the various failure modes with different degree of complexity which occur inside the fiber bundles. Once the damage onset condition is reached, the mechanical performance of the material begins deteriorating. Instead of the traditional direct stiffness reduction scheme [4], continuum damage models (CDMs) based upon the pioneering work of Kachanov et al. [16] are widely adopted to characterize the softening behavior during the damage accumulation process. Besides modelling the elastic damage constitutive behavior for a large range of long fiber reinforced composites [2,3,5,7,8,10,12–15,17], the implementation of CDMs has also been coupled with elastoplastic [18] and viscoelastic-viscoplastic [19] frameworks.

Regarding geometrical modelling strategy, the most frequently used methodologies to generate the geometry of textile composites are based on a combination of the following features: simplified cross-sectional shape of the yarn [8,11,20–27] (such as lenticular, rectangular, ellipsoidal or some hybrid geometry of these basic patterns), constant cross-section assumption of yarn [8,11,21,22,24–26], functional propagation path of the binder yarn [8,11,21–27] and artificially aligned warp and/or weft yarn columns [8,11,21,22,24–26]. Such a simplified model can generally be created in a parametric manner. It is referred to as “idealized” model as opposed to the “real” model, which is reconstructed from the μ CT image. Nowadays, WiseTex and TexGen are considered as the main software to create the parameterized 2D/3D textile composite model. In [28] the idealized geometric modelling is applied to 3D fabrics with parameterized multilayered weave structure, including orthogonal and angle interlock weaves. In general, such software play a role of a “geometry preprocessor” [14,29] for subsequent mechanical calculations.

Isart et al. proposed an analytical approach to model the internal architecture of 3D woven composites from four key cross-sectional images [20]. The yarns contours on the sections were determined from the CT images while the undulation of the binder yarn was simulated analytically with a sinusoidal function. The obtained effective elastic properties are in a good agreement with the experimental results. But the qualitative stress-state analysis shows a strong dependence on the modelled structure which would further affect the damage and failure response of the material. Resorting to the parameterization modelling approach, Green et al. created a deformation model to simulate the real internal geometry of 3D woven composites with a complex spatial waviness and the flattening effect of the yarns being simulated [17]. With such a model, the tensile stiffness and strength of the structure are predicted accurately and the constituents' failure modes match well with the experimental observation.

There is a clear trend, showing that the higher the degree of details in the modelled geometry, the higher the accuracy of the prediction for the mechanical performance. Therefore, allowing the reconstruction from high-resolution 3D images without destructing the observed sample, X-ray μ CT technique shows a great potential to inspect and visualize the real bulk geometry. A direct modelling method was put forward by Naouar et al. for carbon twill woven fabric to reconstruct the real geometry from the CT images [30]. An image processing technique was applied slice by slice to identify and separate constituents. Starting from the restored yarn's surface, the front algorithm was carried out to mesh the geometry with tetrahedral elements. Theoretically, this approach can be applied for modelling any type of reinforcement, however high computational costs in pre- and post-processing are inevitable due to the vast usage of a tetrahedral mesh to fit the curved surface of the yarn. Furthermore, as the yarn contacting zones are prone to initialize the wedge-like volumes. Numerical inaccuracies are more likely to be aroused due to the degraded elements in such regions. Generally, a thin matrix layer is inserted artificially in between yarns so that each yarn can be meshed independently without any interpenetration [11,14]. Nevertheless, such thin matrix layer either introduced extra bad quality elements or demanded finer element size to mesh. Moreover, the resultant global yarn content would be lowered down with respect to the real material.

As an alternative to idealized, parametric models, a voxel-based approach [31] has been developed for a direct conversion of 3D μ CT images into finite element models. A 3D image of a scanned sample, for instance of a 3D woven composite sample, is preliminarily discretized into a number of cubic subdomains (i.e. voxels) with the following variables attached to each voxel: vector of the principal direction of anisotropy; the degree of anisotropy (a variable used for segmentation, defined in section 3.1); and the averaged grey value (AGV), which reflects the X-ray attenuation of the material. Construction of the finite element models involves assigning a material component (matrix, yarn) to a voxel, as well as a local material orientation for the anisotropic material components. Assigning a material component to a voxel is done based on the values of the attached variables using segmentation procedure. If a segmentation into matrix and yarns is required, without distinguishing warp and weft yarn systems, it can be achieved using the degree of anisotropy and AGV [32]. In the case when the warp and weft yarns need to be modelled as separate components, additional information about the local in-plane orientation angle is used [33]. In both cases, the segmentation is done using a supervised classification method based on the construction of a Gaussian mixture model for the material components.

Strong ability to determine the overall elastic properties of the composite with voxel model has been validated by [17,20,24], but to investigate the material response (non-linear behavior, damage and failure) depending greatly on stress concentration the usage of voxel meshing was suggested to be cautious according to [34]. Damage likely initiates at the yarn contact zones where stress oscillation mostly occurs due to the non-continuity (step-like profile) of the yarn reconstructed structure. Stress field smoothing technique cannot completely eliminate that effect, and sometimes even brings extra damage where the material is originally healthy. Moreover, since the maximum local stress increases with decreasing the voxel size, the refinement of the mesh seems helpless to predict precisely the damage onset [34]. The authors acknowledge this fact; the uncertainty brought by voxel meshing is treated as a systematic error in this article.

This article is organized as follows. Manufacturing process and the mechanical properties determination of 3D orthogonal weave composite are introduced briefly in the next section. 3D continuum damage models for yarn and epoxy are presented subsequently. Next, the principle to reconstruct the real voxel model from the 3D μ CT images is illustrated. In parallel, an idealized model with the key dimensions measured from μ CT data is generated to study the influence of mesoscopic geometrical difference on predicting the linear and non-linear behavior of the composite material. Local stress distribution analysis on chosen yarn is conducted to determine the most effective time cost discretizing scheme prior to the computation of the in-plane elastic properties. Progressive damage analysis is

implemented on $\frac{1}{2}$ UC-size RVC models via user subroutine UMAT in ABAQUS/Standard. The damage propagation history and the overall damage intensity are then investigated quantitatively. The simulation results based on real and idealized geometrical modelling strategies show that the damage process of the composite structure depends greatly onto the reconstruction of the yarn surfaces.

2. Materials and constitutive modelling

The 3D orthogonal woven fabric is studied in this work. As shown in **Fig. 1**, warp yarns are oriented along the Z-direction while the wefts along the Y-direction. Three warp layers are placed alternately with weft ones. Binder yarns, running along the warp direction, interlock the multiple weft layers through the thickness. The manufacturing of the composite panel is described in section 2.1 together with the required test methodologies to measure the mechanical properties of the composite. Continuum damage models for yarn and matrix are incorporated in section 2.2 for numerical simulation usage.

2.1 Manufacturing and mechanical properties determination

The preform of the fabric is made of Owen Corning® SE 1200 Type 30 E-glass roving (see **Table 1**). The areal density of the preform is 1732 g/m^2 and the weave densities along warp (ends count) and weft (picks count) directions are respectively 6.89 and 6.92 yarns/cm. Vacuum infusion technique was employed to impregnate the 3D orthogonal weave preforms. Epolam 5015 epoxy and 5015 hardener (Axson Technology®) were mixed with mass ratio 10:3 for resin preparation. The material properties of fiber and resin are summarized in Table 1. The injection was driven by -0.9 bar pressure and followed by a curing process in an autoclave at $50 \text{ }^\circ\text{C}$ for 2 hours according to the manufacturer's data sheet. No extra compression load acted onto the preform during the cure.

Table 1

The collected material properties of fiber and resin (from manufacturers data-sheets)

Properties	E-glass Fiber	Epolam 5015 Resin
Tensile modulus E_i * (GPa)	72	3
Poisson's ratio ν_i	0.3	0.3
Tensile strength X_{iT} (MPa)	2000	80
Compressive strength X_{iC} (MPa)	1350 [35]**	120 [35]
Density (g/cm^3)	2.6	1.1
Yarn linear density (tex)	300	-
Filament diameter (μm)	16	-
Number of fiber per yarn	600	-

*: The subscript i can be replaced with f (fiber) or m (matrix) to represent different constituents

** : The absent experimental data is obtained from literature due to the material similarity

A through-thickness sample was cut from the finished panel and inspected with a micro-tomographic apparatus. The acquisition of images was accomplished with Ultratom RxSolution® 3D CT system [36]. Nano-focus tube was chosen to produce X-rays at a working voltage of 60 kV and a working current of $70 \mu\text{A}$ without using any additional filter. Flat panel detector of 1920×1536 pixels was utilized as imager and the achieved resolution of the image was $4.07 \mu\text{m}/\text{pixel}$. The 3D image of the examined sample was rebuilt via Avizo® as shown in **Fig. 1**.

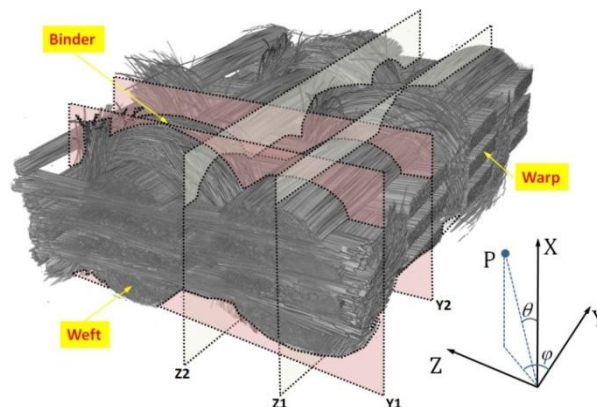


Fig. 1. The structure of 3D orthogonal weave composite with matrix hidden, reconstructed from CT images.

The burn-off test was carried out to determine the overall fiber volume fraction, V_f , of the composite. Five $20 \times$

20 mm² samples, cut from two different composite panels, were burnt at 550°C for 4 hours inside the furnace. The mean V_f is 40.3% with a standard deviation of 0.86%. The definition of the yarn properties in the numerical models requires the intra-yarn fiber volume fraction, $V_{f,Y}$. To authors' knowledge, most of the quantitative approaches to measuring the $V_{f,Y}$ are based upon the treatment of microscale images of the yarn section such as Cross-sectional Area Method [37], Fiber Count Method [37] and the Voronoi Cell Method [38]. In this work, 5 representative zones were picked out all over the weft layers and were recorded by the scanning electronic microscope (SEM). In order to guarantee the representativeness of the intra-yarn fiber content, each representative zone was picked to contain at least 120 fibers. Binarization to the original image makes the fiber components outstanding from the background (i.e. the matrix phase). The median filter was then implemented onto the image to reduce the noise. After wiping off the residual larger spots manually, the $V_{f,Y}$ was determined by dividing the total filament area with the total image area. The mean $V_{f,Y}$ over the chosen weft sections is 75.7% with a standard deviation of 5.2%. The determination of $V_{f,Y}$'s for other yarn components will be introduced in section 3.4 and can be found in **Table 2**.

Standard tensile specimens were machined along weft, warp and 45° direction. The quasi-static loading/unloading tests were carried out on Instron 1185 test machine with a cross-head speed of 3 mm/min. Digital image correlation (DIC) was used to measure the deformation fields on the specimen surfaces by virtue of the commercial DIC software Vic-2D[®]. The tested in-plane mechanical properties will be presented in section 4 with a comparison to those of the numerical prediction results.

2.2 Damage constitution law

Within the frame of continuum damage mechanics, according to the concept of effective stress proposed by Kachanov [16], the effective stress σ^* acting on fictitious undamaged configuration is related to the Cauchy stress σ in actually damaged configuration via a linear operator \mathbf{M} , i.e.:

$$\sigma^* = \mathbf{M} : \sigma \quad (1)$$

\mathbf{M} is a fourth-order damage effect tensor which makes σ^* symmetrized and can be constructed by a second-order symmetric tensor \mathbf{D} , given by Murakami [39] as defined in Eq. (2).

$$\mathbf{D} = \sum d_i \mathbf{n}_i \otimes \mathbf{n}_i \quad (i = 1, 2, 3) \quad (2)$$

\mathbf{n}_i indicates eigenvectors of the damage tensor corresponding to the eigenvalue d_i , a scalar that qualified the net area reduction due to the existence of micro-cavities. In an anisotropic damage model for the yarn, the values of subscript i range from 1 to 3, corresponding to the following failure modes: fiber direction damage, transverse matrix damage along second and third material principal directions. In this article, following \mathbf{M} tensor in Voigt notation is adopted:

$$\mathbf{M}(\mathbf{D}) = \text{diag}[(1-d_1)^{-1}; (1-d_2)^{-1}; (1-d_3)^{-1}; (1-d_4)^{-1}; (1-d_5)^{-1}; (1-d_6)^{-1}] \quad (3)$$

where $d_4 = (d_1+d_2)/2$, $d_5 = (d_1+d_3)/2$ and $d_6 = (d_2+d_3)/2$.

According to the energy equivalence hypothesis proposed by Sidoroff [40], the damaged complementary energy $\Phi(\sigma, d)$ in Eq. (4a) can be obtained by replacing the Cauchy stress σ by the effective stress σ^* in the undamaged complementary energy, i.e. $\Phi(\sigma^*, 0)$ in Eq. (4b). \mathbf{S}^d and \mathbf{S}^0 represent the compliance tensor of the material in damaged and initially undamaged states.

$$\Phi(\sigma, d) = \frac{1}{2} \cdot \sigma : \mathbf{S}^d : \sigma \quad (4a)$$

$$\Phi(\sigma^*, 0) = \frac{1}{2} \cdot \sigma^* : \mathbf{S}^0 : \sigma^* \quad (4b)$$

After the energetic identification, it can be achieved that $\mathbf{S}^d = \mathbf{M}^T : \mathbf{S}^0 : \mathbf{M}$. Correspondingly the damaged stiffness tensor $\mathbf{C}^d = (\mathbf{S}^d)^{-1} = \mathbf{M}^{-1} : \mathbf{C}^0 : (\mathbf{M}^T)^{-1}$ where \mathbf{C}^0 denotes the initial stiffness tensor. Combination with Eq. (3), the \mathbf{C}^d can finally be expressed in Voigt notation as follows:

$$\mathbf{C}^d = \begin{bmatrix} b_1^2 C_{11} & b_1 b_2 C_{12} & b_1 b_3 C_{13} & 0 & 0 & 0 \\ & b_2^2 C_{22} & b_2 b_3 C_{23} & 0 & 0 & 0 \\ & & b_3^2 C_{33} & 0 & 0 & 0 \\ & & & b_{12} C_{44} & 0 & 0 \\ & sym & & & b_{13} C_{55} & 0 \\ & & & & & b_{23} C_{66} \end{bmatrix} \quad (5)$$

In the above matrix $b_i = 1-d_i$ ($i = 1, 2, 3$), $b_{jk} = (2(1-d_j)(1-d_k)/(2-d_j-d_k))^2$ ($j, k = 1, 2, 3$) and C_{mn} ($m, n = 1, 2, \dots, 6$) corresponds to the component in the undamaged stiffness matrix.

2.3 Damage initiation criteria

3D Hashin's criteria as Eq. (6) were formed to detect the fiber failure (d_1) and the in-plane/out-of-plane transverse matrix cracking failure (d_2 and d_3) modes:

$$\begin{aligned} F_{d1} &= \frac{\sigma_{11}^2}{X_{T(C)L}^2} + \alpha_{1T(C)} \left(\frac{\sigma_{12}^2}{X_S^2} + \frac{\sigma_{13}^2}{X_S^2} \right) \geq 1 \\ F_{d2} &= \frac{\sigma_{22}^2}{X_{T(C)T}^2} + \alpha_{2T(C)} \left(\frac{\sigma_{12}^2}{X_S^2} + \frac{\sigma_{23}^2}{X_S^2} \right) \geq 1 \\ F_{d3} &= \frac{\sigma_{33}^2}{X_{T(C)T}^2} + \alpha_{3T(C)} \left(\frac{\sigma_{13}^2}{X_S^2} + \frac{\sigma_{23}^2}{X_S^2} \right) \geq 1 \end{aligned} \quad (6)$$

F denotes the value of the damage function, σ_{ij} ($i, j = 1, 2, 3$) are the stress components in the local material coordinates system. X_{TL} , X_{CL} , X_{TT} , X_{CT} denote the tensile/compressive strength (T/C in the first slot of the subscripts) along longitudinal/transverse direction (L/T in the second slot of the subscripts) of the transversely isotropic yarn while X_S indicates the shearing strength. Particularly, $\alpha_{T(C)}$ is introduced here to take the shear contribution into account with the value ranging from 0 to 1.

2.4 Damage evolution law

Finite element method is most frequently employed to carry out damage simulations for composite materials in general and, in particular, for 3D textile reinforced composites. In order to minimize the mesh dependency on dissipated fracture energy during the damage process, regularization scheme based on Bažant's crack band model [41], which associates the critical strain energy release rate $G_{I,c}$ (in J/m^2) with the characteristic dimension L^* of the finite element, has been implemented to model different types of strain-softening behavior: for linear mode [5,7,8,10,13] and for exponential mode [3,17,19,42]. The exponential damage evolution law is established here as expressed as follows:

$$d_i = 1 - \frac{1}{f_{di}} e^{(1-f_{di})X_I^2 L^*/(E_i G_{I,c})} \quad (i = 1, 2, 3; I = T(C)L \text{ if } i = 1, \text{ else } I = T(C)T) \quad (7)$$

The damage state variable d_i varies from 0 (the undamaged state) to 1 (the fully damaged state, indeed 0.999 is used to avoid the singularity of damaged stiffness matrix) and proportional to the failure index f_{di} increasing from damage onset to final failure of the material. f_{di} are calculated as the square root of the damage functions F_{di} . The value of $G_{I,c}$ depends on the damage modes of the yarn: for the longitudinal direction it is equal to $G_{T(C)L,c}$ and for the transverse direction, $G_{T(C)T,c}$. In this work, since only tensile behaviors are studied, the fracture toughness $G_{TL,c}$ and $G_{TT,c}$ are equal to 60.0 and 1.5 kJ/m^2 respectively (the data is collected from [11] due to the material similarity). E_i represents the undamaged modulus perpendicular to i -th failure plane.

Since the degradation of the damaged material often results in numerical convergence difficulties, viscous regularization scheme is implemented to guarantee the positive tangent stiffness matrix within a tiny time increment Δt . The regularized damage variable d_i^v in $(n+1)$ -th increment can be evaluated by Eq. (9) and used to update the damaged stiffness matrix instead of d_i which evaluated from Eq. (8); η denotes the viscous regularization parameter.

$$d_i^v \Big|_{t^{n+1}} = \frac{\Delta t}{\Delta t + \eta} d_i \Big|_{t^{n+1}} + \frac{\Delta t}{\Delta t + \eta} d_i^v \Big|_{t^n} \quad (i = f, m1, m2) \quad (8)$$

Therefore it can be derived that,

$$\frac{\partial d_i^v}{\partial d_i} = \frac{\Delta t}{\Delta t + \eta} \quad (9)$$

At last, the Jacobian matrix of the damaged material can be formulated as follows:

$$\frac{\partial \sigma^*}{\partial \varepsilon} = C^d + \frac{\Delta t}{\Delta t + \eta} \left(\sum_i \frac{\partial C^d}{\partial d_i^v} \varepsilon \frac{\partial d_i}{\partial \varepsilon} \right) \quad (i = f, m1, m2) \quad (10)$$

3. Reconstruction of real geometry

The supervised classification scheme is integrated into the voxel-based modelling algorithm proposed in [31] to

improve the segmentation of material domains. The method is explained in section 3.1 by taking 3D woven composite as an example. A comparable idealized UC model is created via parameterization technique in section 3.2. The comparisons focused on yarn morphology, local orientation of yarn and the fiber and/or yarn volume fraction are conducted in section 3.3-3.4.

3.1 μ CT scans analysis and voxel model generation

A region of interest (ROI) of $2.76 \times 2.76 \times 1.98 \text{ mm}^3$, which is taken as a UC, is picked out from the 3D μ CT image for reconstruction. Following the treatment procedure suggested by Straumit et al. in [31], the 3D image domain is partitioned into a number of voxels by imposing a regular rectangular 3D mesh on the μ CT image. Two scalar variables are assigned to each voxel at the end of the discretization stage: average grey value and the degree of anisotropy. The average grey value (AGV) is estimated as an average of the grey value in the image over the voxel domain. The degree of anisotropy β is calculated as follows:

$$\beta = \begin{cases} 1 - \frac{\lambda_1}{\lambda_3} & \lambda_3 > 0 \\ 0 & \lambda_3 = 0 \end{cases} \quad (11)$$

where $\lambda_1 \leq \lambda_2 \leq \lambda_3$ are the eigenvalues of the structure tensor (refer to [31] for the definition of the structure tensor). The plot of the degree of anisotropy versus the average grey value roughly outlines two clusters (**Fig. 2**): the lower left with lower anisotropy and lower AGV is identified as the matrix phase while the top right is associated with the raw yarns and needs a refined analysis. The eigenvector \mathbf{v}_1 corresponding to λ_1 is taken as the principal direction of the anisotropy owing to the implication of minimum variability. Further projection of \mathbf{v}_1 onto the weaving plane (i.e. YZ plane in **Fig. 1**) yields two peaks in the histogram of the azimuthal angle ϕ (**Fig. 3**). This feature renders the possibility to subdivide the yarns along weft ($\phi = 0^\circ$) and warp ($\phi = 90^\circ$, binder yarns are also contained) direction.

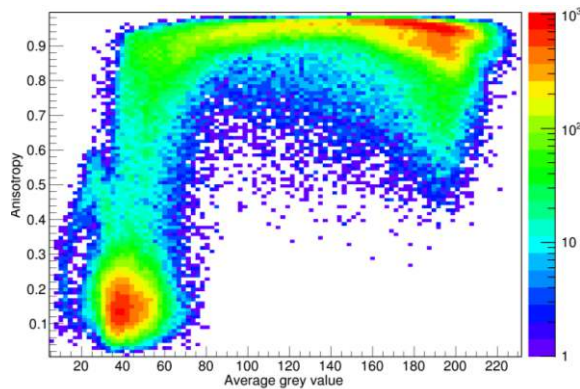


Fig. 2. Histogram of the degree of anisotropy versus average grey value computed from the real UC model with 10-pixel voxel size.

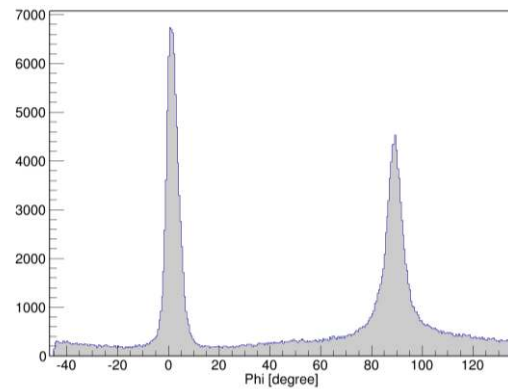


Fig. 3. Histogram of ϕ (Phi) angle on YZ projection plane computed from the real UC model with 10-pixel voxel size.

Segmentation via two-parameter K-means clustering algorithm, as well as via thresholding method, faces the dilemma of either misclassification of material phases or impossibility for subdivision of raw yarn cluster. Among all the available strategies to overcome this problem, example-based supervised classification algorithms (such as [43]) seem to be the more efficient. The implementation of such an algorithm requires a database consisting of typical examples, further called a “training set”, each of which is in form $\{(\mathbf{X}_i, \text{Label}_i), \dots, (\mathbf{X}_n, \text{Label}_n)\}$ where \mathbf{X}_i represents the i -th feature vector and Label_i corresponds to its category. The classifier is then trained on the example data by approximating the feature vector distributions in each category with multivariate Gaussian distributions, thus forming a Gaussian mixture model [44]. The segmentation is done by computing probabilities for a voxel to belong to each of the material components, and the component with the highest probability is assigned to the voxel [33].

Three training examples are used to identify the matrix, weft and warp constituents by using feature vector in form of $(\text{AGV}, \beta, \phi)$. The training examples are 3D ROIs, selected from the image so that to contain a single material component. Supervised by the examples, aforementioned unit cell ROI is converted into a voxel model (10-pixel voxel size) as shown in **Fig. 4** (the matrix material is hidden). It is worth noting that the reconstruction makes the original warp and binder yarns merge together due to the close feature vector. The new yarn group (the element set in

green in **Fig. 4**) is named as “collective warps” in this article. Note that the local orientations are assigned per voxel and hence are not affected by this merge.

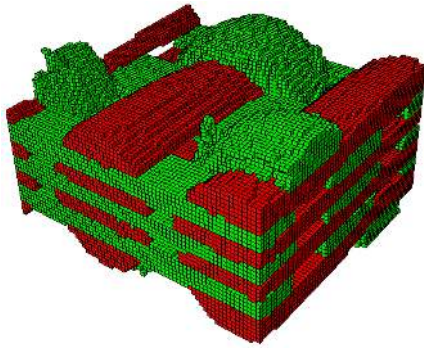


Fig. 4. The real voxel UC model (with the matrix hidden), created from the CT image.

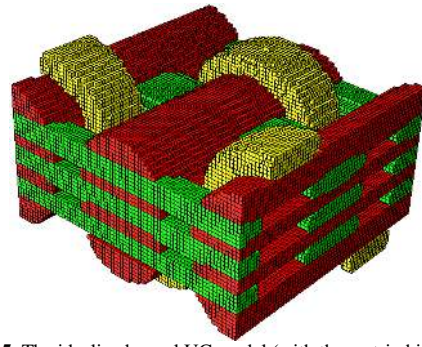


Fig. 5. The idealized voxel UC model (with the matrix hidden).

3.2 Parameterized modelling

An idealized UC (**Fig. 5**) model, with the same resolution as in the real model, was created by parameterization to evaluate the influence of geometry on the prediction of effective properties. The key morphological and geometric parameters of the yarns were measured directly from the μ CT images. The sections of the yarns, including binders, warps and the wefts in the two middle layers, are fit with a power ellipse while the wefts on top and bottom are adapted by using lenticular-rectangular-hybrid shape. The variation of section owing to the contact interaction between yarns during weaving process is simulated for binders and wefts. The undulation of binder yarn is defined by an 11-knot-B-spline curve. Local orientation of each element was derived inherently according to the centerline of the yarn. The generation of the idealized model is implemented in TexGen via Python script code.

3.3 Geometric comparison

Four typical sections Y1, Y2, Z1 and Z2 defined in **Fig. 1** are taken as benchmarks onto which the generated yarn profiles of real and idealized models will be superposed. The contrast charts on above sections are depicted in **Fig. 6- Fig. 7**. For idealized sections, the yellow zones outline the cross-section of binder yarns while the red zones depict the wefts and the green ones indicate the warps. The real sections are in grey color because of the excellent fit results for both the shape and the undulation path.

The average yarn dimensions measured in the μ CT images are fit to the real geometry locally, (for example the compaction effect on the top and bottom of binder), but fail to take into account exactly the thickness variation along the yarn path (**Fig. 6a**). Simplified sectional shapes (like ellipse, lenticular, power ellipse or a hybrid shape) encounter difficulties to approximate the real yarn (**Fig. 6b**). In addition, the artificially selected number and position of the interpolation points to define the B-spline curve also influences considerably the binder path (**Fig. 6a**).

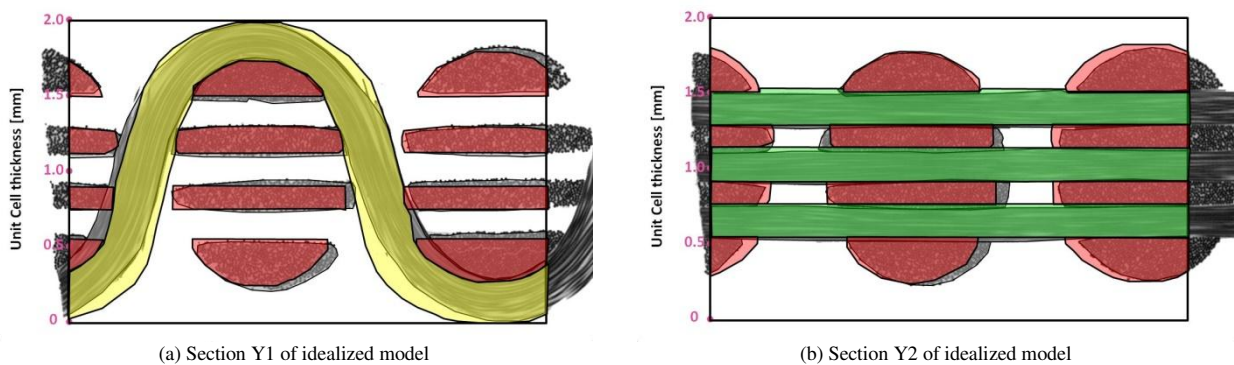


Fig. 6. Generated Y1 and Y2 sections of idealized (colored)/real (grey) models superpose onto the real geometry.

Similar conclusions can be made for Z1 and Z2 sections. In the real model, the thickness variation of the weft yarns is well characterized and the warp yarns are accurately represented in both shape and area aspects. By contrast, for the idealized model, the waviness of weft resulting from the compacting of the binder is poorly modelled (**Fig. 7a**). In addition, the constant thickness assumption of the binder yarn fails to simulate the real thickness variation in

between the two weft columns and causes an unrealistic projection area on Z2 section (**Fig. 7b**).

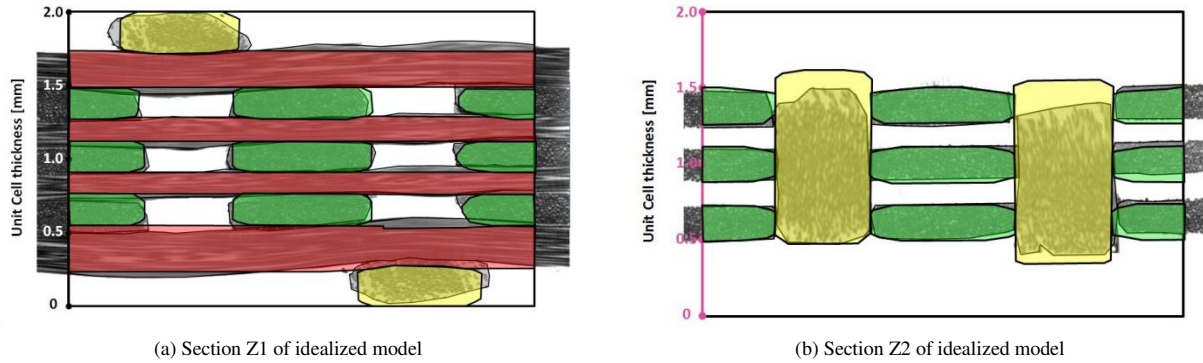


Fig. 7. Generated Z1 and Z2 sections of idealized (colored)/real (grey) models superpose onto the real geometry.

3.4 Yarn/fiber content comparison

A fine discretization scheme with a voxel size of 5 pixels is imposed on the image to reconstruct the real model so that the yarn volume fraction (V_Y), obtained upon the segmentation, can be taken as a reference for the idealized model. As given in **Table 2**, the $V_{f,Y}$ of weft (75.7%) is fixed for both models to make them as comparable as possible. Particularly, in the idealized model the $V_{f,Y}$ of warp is assumed to equal to that of weft. The unknown $V_{f,Y}$'s of the collective warps in the real case, and of the binders in the idealized case, were determined by the reverse method to reach the same overall fiber content as the experimental value (40.3%). Generally speaking, from the point of view of constituents' properties, the generated models match well with each other except for some slight allocation differences on V_Y . It should be pointed out that in further real sub-UC models the $V_{f,Y}$ for each component will keep the same value as in real UC.

Table 2
Fiber/Yarn/Intra-yarn fiber volume contents in real and idealized UC models.

		Real UC model		Idealized UC model	
Weft yarn		$V_Y=27.4\%$	$V_{f,Y}=75.7\%$	$V_Y=27.0\%$	$V_{f,Y}=75.7\%$
Collective Warps (Real)	Binder (Idealized)	$V_Y=28.0\%$	$V_{f,Y}=69.9\%$	$V_Y=9.4\%$	$V_{f,Y}=58.1\%$
	Warp (Idealized)			$V_Y=19.0\%$	$V_{f,Y}=75.7\%$

The blue short lines in **Fig. 8** show the fiber directions in each voxel. The derived local orientations perform good tangency to the real curved profile in each part of the yarn.

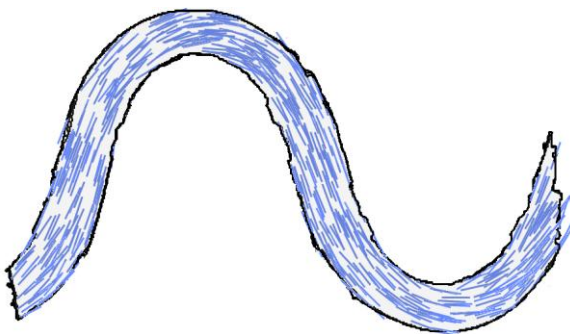


Fig. 8. The computed local fiber orientations distribute along the binder path.

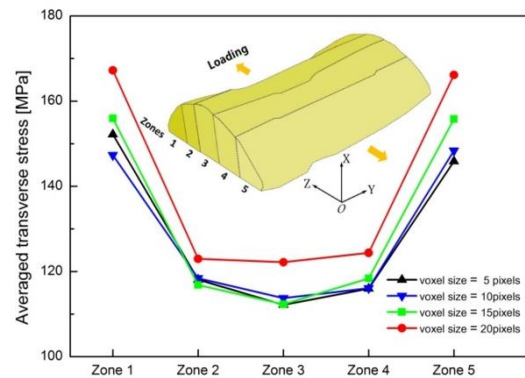


Fig. 9. Averaged transverse stress distributes along weft width in different voxel size cases.

4. Results and discussion

4.1 Mesh density study

Four voxel sizes that range from 5 to 20 pixels are chosen to discretize the real UC volume. An overall tensile strain of 1% along the warp direction is imposed to model a simple tension test. After solving the elastic boundary value problem, a weft yarn that interlaces directly with the binder is picked out and divided into five strip zones

along the tensile direction, as illustrated in **Fig. 9**. The in-plane transverse stress is averaged over each strip and the convergence of the averaged stress distributing along the width direction is studied to determine a reasonable mesh density for effective properties prediction.

All the curves in **Fig. 9** catch the feature that higher in-plane transverse stresses occur at the two lateral zones (Zone 1 and 5) while in middle strips the stress is only 72%-80% of the peak stress. Due to the interaction during compaction of the reinforcement, the edge of the weft is severely squeezed, which induces a high-stress concentration region and consequently enhances the overall stress level of the zone. The averaged stress falls 5%-8% when the voxel size decreases from 20 to 15 pixels. As the size keeps decreasing, convergence firstly appears to happen in the three middle zones where the yarn geometry changes smoothly. In the end, the maximum error between 5 and 10 pixels cases has been confined within 3.3%, but with a 140 times higher CPU computation cost than the latter one (Remark: all the simulations in this paper were run on a workstation with a 4-core Xeon CPU X5550, 2.67 GHz and 8 GB RAM). Based upon the tradeoff between computational efficiency and predictive accuracy, 10-pixel-length voxel discretization scheme is chosen for all the following simulations.

Due to the fact that the homogenized stiffness matrix is derived from the averaged stress components, the mesh density exerts little influence on predicting the effective elastic properties, as long as the convergence for the voxel size is reached. However, this is not the case when simulating the damage behavior. **Fig. 10** shows the in-plane transverse stress fields viewing from the top of the chosen yarn under four discretization schemes as mentioned above. ‘‘M’’ indicates the element where maximum stress occurs. By observation, the maximum stress mostly takes place in the isolated element(s). The geometric features of the yarn are reproduced increasingly detailed as the mesh turns finer, and the characteristic profile of stress contour turns clearer. During this process, the location of the stress maximum shifts to different parts of the model. It means that a voxel-based damage simulation will be mesh dependent and according to Doitrand et. al [34], it cannot even be avoided. Therefore, in this study, the voxel-based damage simulation will focus more on describing qualitatively the influence of the geometrical difference between real and idealized models.

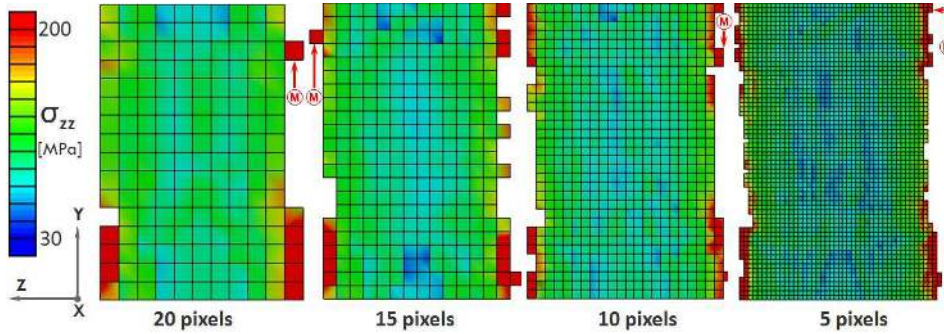


Fig. 10. Transverse stress fields on the surface of weft yarn obtained with different voxel sizes (top views).

4.2 In-plane effective properties

Six independent loading cases were carried out for elastic properties determination of real and idealized models. The macroscopic deformation tensor $\overset{(ij)}{\varepsilon}_{kl}$ under a specified loading case is defined as:

$$\varepsilon_{kl}^{(ij)} = \delta_{ik}\delta_{jl}\varepsilon_{ij}^0 \quad (i, j, k, l = 1, 2, 3). \quad (12)$$

ij in the parenthesis indicates the loading case in which the global deformation $\overset{0}{\varepsilon}_{ij}$ is acted. δ is the Kronecker symbol. Two types of strain-controlled boundary conditions (BCs) are able to realize Eq. (12): the Kinematic uniform boundary conditions (KUBCs) and the Periodic boundary conditions (PBCs). Considering a volume element V , \mathbf{x} is an arbitrary point on the boundary ∂V , for KUBCs, the displacement field u_i can be expressed as follows:

$$u_i = \varepsilon_{ij}^0 x_j. \quad (13)$$

The homogenized strain $\overline{\varepsilon}_{ij}$ and stress $\overline{\sigma}_{ij}$ tensors can then be derived as Eq. (14) where the volume averaging scheme was employed.

$$\overline{\varepsilon}_{ij} = \frac{1}{V} \int_V \varepsilon_{ij} dV = \varepsilon_{ij}^0 \quad \text{and} \quad \overline{\sigma}_{ij} = \frac{1}{V} \int_V \sigma_{ij} dV \quad (14)$$

For PBCs, as indicated in Eq. (15), u^* is the unknown displacement function to represent the periodic variation of each opposite face/edge pair on ∂V and it takes the same value at the two homologous points on the opposite faces.

$$u_i = \varepsilon_{ij}^0 x_j + u_i^* \quad (15)$$

Additionally, since the traction vector $\sigma_{ij} n_j$ is of the same magnitude but opposite orientation at two corresponding points, following relationship can be inferred:

$$\overline{\varepsilon}_{ij} = \varepsilon_{ij}^0 \quad \text{and} \quad \int_V \sigma_{ij} u_{i,j}^* dV = 0. \quad (16)$$

Due to the rigorous requirement of periodic geometry, PBCs are applied only to the idealized models in this work. As to the real models, KUBCs are imposed alternatively. The volume averaging theory was carried out to calculate the effective stress component $\overline{\sigma}_{ij}$:

$$\overline{\sigma}_{ij} = \frac{1}{V} \iiint_V \sigma_{ij} dV = \frac{1}{V} \sum_{ne} \iiint_{V^e} \sigma_{ij} dV^e = \frac{1}{V} \sum_{ne=1}^{NE} \sum_{ip=1}^{NI} \sigma_{ij}^{ne}(ip) \cdot W^{ne}(ip) \cdot J^{ne}(ip) \quad (17)$$

where NE (NI) is the total number of an element (Gaussian integration point, IP) in the model (each element), $\sigma_{ij}^{ne}(ip)$ indicates the stress component on a certain integration point while $W^{ne}(ip)$ and $J^{ne}(ip)$ denote respectively the weight value and the Jacobian determinant value corresponding to that IP. A Python post-process script is written to calculate the effective elastic properties. Details of the homogenization procedure implemented in this article has been reported in [26].

For the idealized model, the predicted effective moduli based on PBCs are preferred than on KUBCs, although after homogenization the maximum difference about the moduli via these two BCs is less than 1%, as the former has taken into account the periodic repetition of the geometry and inherently guaranteed the stress continuity on the opposite boundaries.

The effective moduli E_{warp} , E_{weft} and E_{45° for real and idealized models are summarized in **Table 3** with relative errors to the experimental values. The randomly dispersed breakage of glass fiber caused by fabric manufacture and/or transportation mainly results in the scattered experimental data. In addition, the limited machining accuracy of the specimen would also aggravate the scatter, especially for the 45° ones. In this study, the maximum coefficient of variation (COV, the ratio of the standard deviation and the mean value) reaches up to 4.8% for warp direction tensile moduli measurement which is likely lead by the irregular distribution of local breakage inside the binder yarn (refer to **Fig. 1**).

Table 3
The predicted in-plane effective properties of real and idealized models

	Experimental	Idealized UC	Real UC	Real 1/2 UC	Real 1/4 UC
E_{warp} (GPa)	16.1 (COV 4.8%)	15.8 (-1.3%)*	15.4 (-4.2%)	15.8 (-1.6%)	15.8 (-1.4%)
E_{weft} (GPa)	20.3 (COV 3.0%)	21.0 (+3.6%)	19.9 (-1.7%)	20.0 (-1.0%)	19.9 (-1.9%)
E_{45° (GPa)	10.7 (COV 3.5%)	10.2 (-4.3%)	10.6 (-1.2%)	10.7 (+0.6%)	10.6 (-0.4%)

* The percentages for numerical prediction indicate the relative deviation compared with the mean experiment value.

For idealized UC model, the predicted E_{warp} is 1.3% lower than the experimental value. Meanwhile, E_{weft} and E_{45° are estimated with relatively higher deviation from the measured values. By contrast, the real UC model presents better approximation on E_{weft} and E_{45° with only 1.2-1.7% underestimation but yields a higher error of -4.2% for the E_{warp} .

As to the sub-UC models, cutting manners are illustrated schematically in **Fig. 12** and will be remarked as 1/4 UC or 1/2 UC model according to their size in the following, all the predicted in-plane moduli match well with the experimental results with absolute errors ranging from 0.4% to 1.9%. **Fig. 12** shows the trend of CPU time cost for computation against the homogenization strategies. The idealized UC is proved to be the most time-consuming scheme. For real UC, although the accuracy is enhanced a little, the computation cost has been saved little as the total degree of freedom (DOF) of the model remains almost unchanged. Real sub-UC homogenization strategies are thus strongly suggested to determine the effective elastic properties for they provide an excellent agreement compared with the full UC models (time cost of 1/8-1/4 compared to the full models).

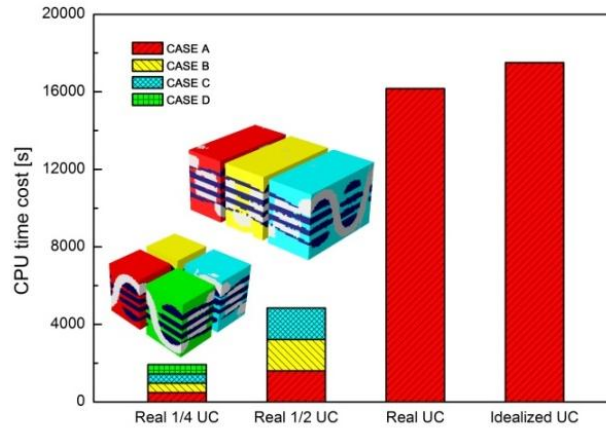


Fig. 11. CPU time cost versus homogenization strategies.

4.3 Progressive damage analysis

Two typical configurations, similar to Case A and B in **Fig. 11**, of $\frac{1}{2}$ UC model, were reconstructed for both real and idealized modelling strategy. The influences of the modeled geometry on predicting the progressive damage behavior were then investigated by loading the models along warp direction. The required yarn strength properties, as listed in **Table 4**, were estimated by a combination of Rosen's [14] and Chamis' [45] analytical models. The shear contribution factors in Eq. (6) were set to be zero in this article hence 3D Hashin's damage initiation criterion is degraded into the maximum stress criterion. In addition, the damage of matrix (d_m) is detected by maximum principal stress criterion, once the damage occurs at the material point the stiffness reduces to 0.001 of the undamaged value.

Table 4

The input data of different yarns' strength estimated by Rosen's ($X_{TC,L/T}$) [14] and Chamis' model (X_S) [45].

$V_{f,y}$ of yarn	$X_{T,L}$ (MPa)	$X_{C,L}$ (MPa)	$X_{T,T}$ (MPa)	$X_{C,T}$ (MPa)	X_S (MPa)
58.1% (Idealized binder)	1195.5	2603.4	124.4	186.6	33.1
69.9% (Real collective warps)	1422.1	3945.2	121.1	181.7	34.8
75.7% (Idealized warp and all wefts)	1533.4	4202.8	117.0	175.5	35.7

Fig. 12 (left-y-axis) shows the simulated tension curves and the upper and lower bounds of the experimental tests. The predicted peak values of stress and the corresponding ultimate strain are summarized in **Table 5**. As can be seen clearly, the modelling strategy (real/idealized) manifests higher impact on the strength prediction than the unit cell size (full or $\frac{1}{2}$ UC). The idealized models tend to predict the strength by 31% higher than the experimental value while the real ones present the results with only a difference of 1.3%. In the elastic stage, i.e. while the tensile strain less than $\sim 0.30\%$, all the simulated curves overlap together inside the experimental range. Two branches were observed thereafter, the idealized ones run above the experimental upper bound; the real ones keep close to the upper bound up to the strain reaches 1.64% then the material softening accelerates until the final failure. This phenomenon reveals that the damage evolution history of the idealized and real models may differ from each other.

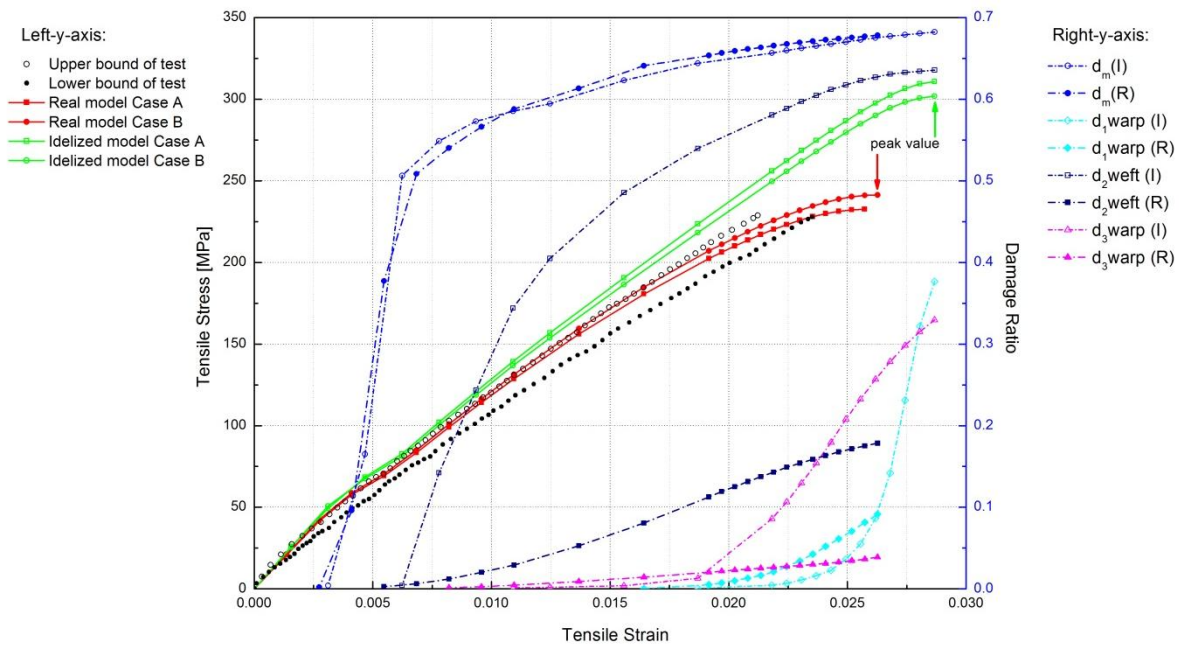


Fig. 12. Simulated stress-strain curves along with the experimental upper and lower bounds (Left-y-axis); evolution history of d_i in matrix/collective warps/wefts component (Right-y-axis).

Table 5

The predicted tensile strength and strain of $\frac{1}{2}$ UC models and the experimental results (loading along warp direction).

	Real Case A	Real Case B	Idealized Case A	Idealized Case B	Experiment
Tensile strength (MPa)	232.6	241.3	310.8	301.8	$233.8 \pm 1.7\%$
Tensile ultimate strain	0.0257	0.0263	0.0287	0.0287	$0.0227 \pm 4.6\%$

In order to investigate these differences in detail, post-treatment procedure was implemented on Case B of I/R models, I/R is short for idealized/real. A scalar quantity “damage ratio” is proposed here to describe how much volume fraction of the material gets damaged, and it is defined as $N_{m,di}/N_{m,total}$, where N denotes the number of elements, m stands for the material component and can be taken as matrix/collective warps/wefts and d_i indicates the damage modes. The concept “collective warps” is borrowed from the real modelling strategy to represent all the yarns travelling along the warp direction inside the idealized models. The damage ratio of each material component was plotted against the tensile strain so that the active damage scope can be illustrated quantitatively, as shown in **Fig. 12** (right-y-axis). Four dominating damage modes during the tension will be discussed below.

Since the damage ratio of the matrix shows little dependence on modelling strategy, as presented in **Fig. 12** (right-y-axis, solid/open circular symbols in blue), the matrix damage process of the real model is analyzed as an example. A few damaged elements were first detected in the vicinity of the binder boundary at the strain of 0.27% (**Fig. 13a**). The number of the damaged element increases quickly through the model thickness as the tensile strain proceeds to 0.68%, consequently, 50.8% of the matrix elements failed to bear the loading due to the large penalty coefficient (**Fig. 14b**). The rapid spread of damage directly leads to the first slope change of the stress-strain curve. After this critical strain, the damage ratio grows slower and tends to converge toward a value around 0.7. The damage propagates mainly along the warp direction. The predicted damage process agrees well with the results reported in [3] where damage behavior of matrix for the similar structure was studied numerically.

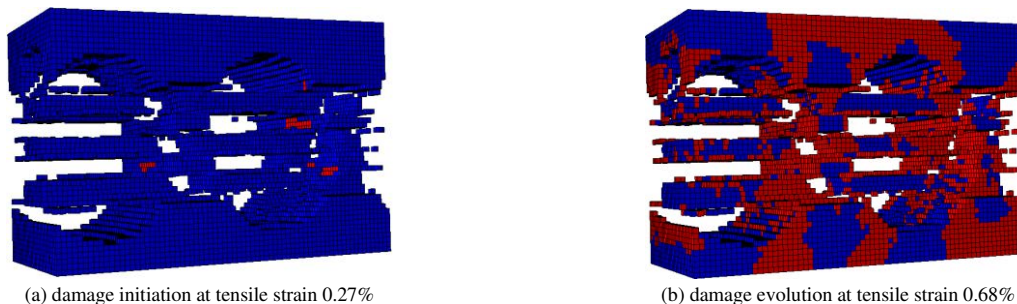


Fig. 13. The matrix damage process of real model: the healthy elements are colored in blue while the damaged are in red.

In-plane transverse matrix cracking (d_2) takes place inside the wefts for both I/R models after the d_m stepped into

middle-late evolution stage, as shown in **Fig. 12** (right-y-axis, solid/open square symbols in navy). The damage initiated at the edges of the wefts and propagated towards the yarn center. In spite of the similar damage propagation paths, the damage ratio histories differ apparently from each other. When the peak values of stress were reached respectively, 63.6% of the wefts got damaged in the idealized model while only 17.9% was found in the real one. Interestingly, during the evolution process of d_2 , the larger damage scope of the idealized model does not help to reduce the gap between the tensile curves of I/R models, which implies that higher damage intensity probably exists inside the real model.

Fig. 14 plots the statistical distribution of the d_i ($i=1, 2, 3$) values over all the damaged elements in wefts or collective warps at the ultimate strain. The characteristic damage contours at that moment are shown in each plot. The distribution of the d_i variable, which ranges from 0.0 to 1.0, is shown as a histogram with 20 bins (0.5 bin size). Such a plot allows statistical characterization of the damage intensity hence is considered to be complementary with the classic damage contours.

As presented in **Fig. 14a**, (0.75, 0.85) is the most intensive distribution interval for the idealized model, containing 35.5% of the damaged weft elements. For the real model, this interval is (0.80, 1.0) with 37.3% of the damaged elements included. Referring to the damage contours, the idealized model yields a more continuous distribution of d_2 than the real one. The lower variation of the yarn geometry facilitates the stress transfer along the loading direction and results in a larger damage scale, but a lower damage level. By contrast, the damaged elements in the real model were found to aggregate at the weft surfaces and the localized damage zones were formed there. As the strain increases, the indented surfaces of the reconstructed yarns are apt to arrest the damage and to intensify the local damage level.

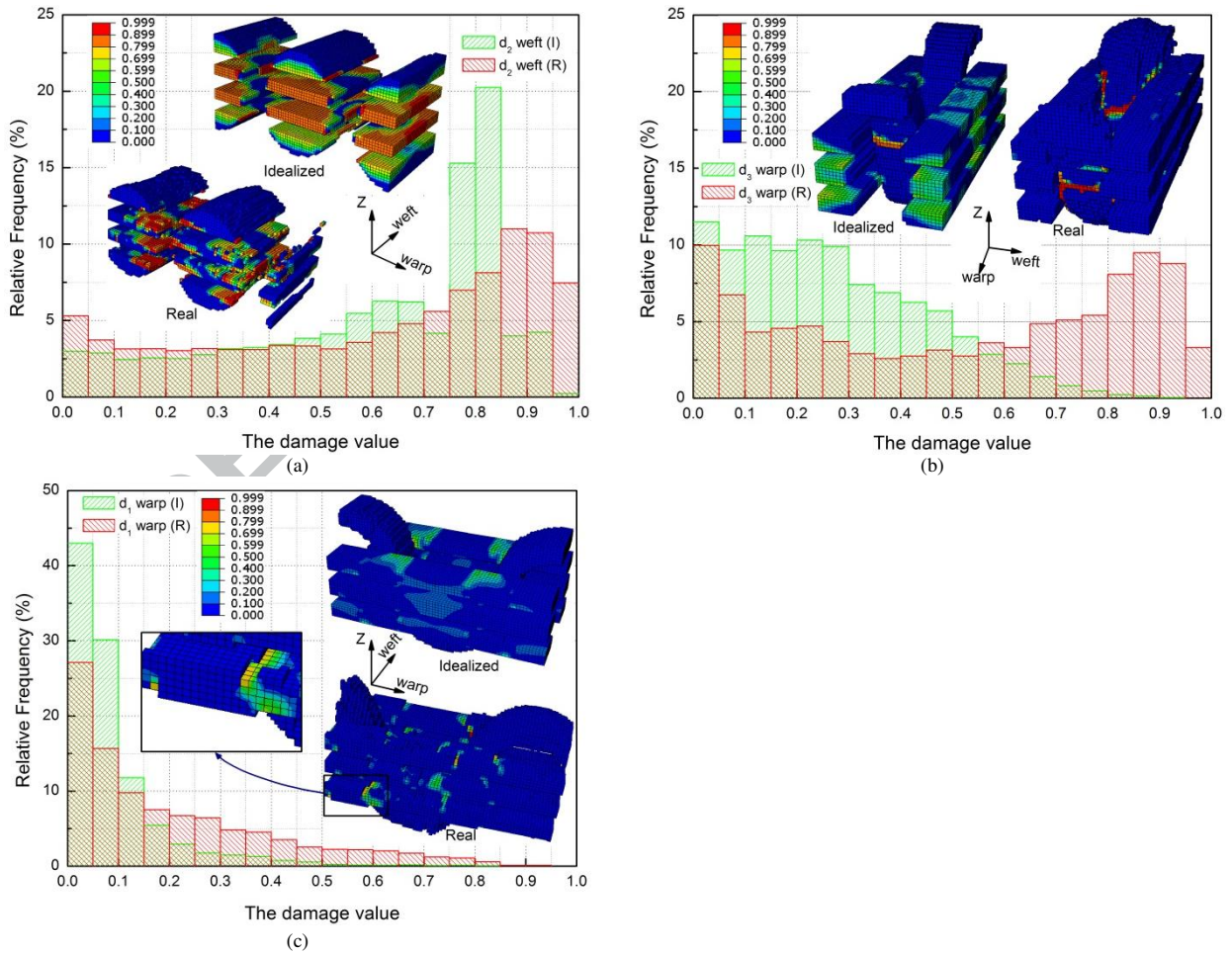


Fig. 14. The statistical distribution of the damage value at the time when peak stress value is reached: (a) transverse matrix crack in wefts (d_2); (b) delamination of yarn in collective warps (d_3) and (c) yarn breakage in the warps (d_1).

The out-of-plane transverse matrix cracking (d_3) of collective warps initiates later than the occurrence of d_2 in wefts, as shown in **Fig. 12** (right-y-axis, solid/open triangular symbols in magenta). In idealized model, a kink point at strain 1.87% segments the damage evolution process into two stages: (I) damage appears on the binder surface and

grows slightly along the width; (II) damage diffuses into the warps leading to the rapid increase of the damage ratio from 1.3% to 33.0%. At the end of stage II, 61.5% of the damaged elements have a d_3 value less than 0.3, while few elements (if any) are detected with damage value included between (0.85, 1.0) (**Fig. 14b**). However, for the real model, the damage ratio grows gently to 4.2% without any visible kink point. The overwhelming majority of the damage is restrained within the binder and few of them propagate into the warps (**Fig. 14b**). This localized damage position coincides with the site where the pre-breakage of the binder is located in the raw material sample, as can be seen in **Fig. 1**. Furthermore, the unevenness of the reconstructed binder deepens the damage level that 29.6% of the damaged elements were detected with the d_3 value falling inside the interval (0.85, 1.0).

The breakage of yarn (d_1) is the last occurred damage mode in I/R models, as shown in **Fig. 13** (right-y-axis, solid/open diamond symbols in cyan). It initiates in the warps at the regions where contact with the binder. In the idealized model, as the strain proceeds, damage diffuses regularly from the position where the initial damage takes place, towards the width of the warp. Since the initiation, the damage propagates increasingly fast until 36.7% of the collective warps get damaged while reaching the peak stress. The left-skewed distribution of damage value in **Fig. 14c** implies small overall damage intensity. For the real case, the already-formed damage propagates along the yarn width slightly, while new damage appears wherever the non-smooth surfaces are reconstructed, as schematically shown in the enlarged view in **Fig. 14c**. It is emphasized again that the real model tends to show a lower damage ratio but a higher damage degree.

5. Conclusions

Reconstructed from the μ CT images, real models of a 3D orthogonal woven composite were compared with the conventional parametric modelling scheme. The real strategy allows a high-fidelity reconstruction of the composite meso-structure, including the waviness of the yarns, the variation of yarns' thickness, the complex shapes of the yarn cross sections and the unevenness of yarn surfaces. The reproduced models shortened the gap to the real material on both geometry and constituents' property aspects. Yarns are subdivided into collective warps and wefts according to the feature vector (AGV, β, φ) so that for different yarn components the material properties can be assigned separately.

The performance of the real models and the idealized ones is examined via the homogenization of in-plane properties and via the simulation of the damage and failure process. The accuracy in prediction of effective properties using real models is higher in comparison with idealized ones. Moreover, the superiorities of the real models have been sufficiently demonstrated in progressive damage analysis. The predicted modulus and strength are within the range of experimental data. At meso-scale, the underlying factors, which help to present the good agreement with the practical tensile performance, were investigated in a quantitative manner. Compared to the smoother surface of yarn in idealized model, the rougher one in real model is more prone to cause the stress concentration, where the damage is most likely to initiate. As the macroscopic deformation increases, the damage propagation on yarn surface would be mainly confined inside such unsmooth regions; as a result the accumulation of damage gets augmented there locally. This explains the smaller damage scope but higher damage degree occurred in the real model. Notably, the voxel model is apt to deepen the damage localization due to the step-like discontinuous surfaces.

Acknowledgement

One of the authors, Yang LIU, wishes to acknowledge sincerely the financial support of the China Scholarship Council such that this research can be undertaken. Stepan V. Lomov is a Toray professor (Toray Chair for Composite Materials in KU Leuven). The Nord-Pas-de-Calais Region and the European Community (FEDER funds) partly funds the X-ray tomography equipment. The reconstruction of the real models in this article are realized by taking advantage of VoxTex software which was developed with a support by the European Union's Seventh Framework Programme for research, technological development and demonstration under Grant Agreement No. ACP2-GA-2012-314562-QUICOM. Part of the presented results was achieved within the project JOINing of copper to aluminium by ElectroMagnetic fields – "JOIN'EM" which is funded by the European Union within the frame of the Horizon 2020 research and innovation program under Grant Agreement No. 677660.

References

- [1] Mouritz AP, Bannister MK, Falzon PJ, Leong KH. Review of applications for advanced three-dimensional fibre textile composites. *Compos Part A Appl Sci Manuf* 1999;30:1445–61.

- [2] Zhang C, Li N, Wang W, Binienda WK, Fang H. Progressive damage simulation of triaxially braided composite using a 3D meso-scale finite element model. *Compos Struct* 2015;125:104–16.
- [3] Dai S, Cunningham PR. Multi-scale damage modelling of 3D woven composites under uni-axial tension. *Compos Struct* 2016;142:298–312. doi:10.1016/j.compstruct.2016.01.103.
- [4] Ahn H, Yu W-R. Mechanical analysis of 3D braided and woven composites using fiber-based continuum analysis. *Compos Struct* 2016. doi:10.1016/j.compstruct.2016.11.003.
- [5] Fang G, Liang J, Wang B. Progressive damage and nonlinear analysis of 3D four-directional braided composites under unidirectional tension. *Compos Struct* 2009;89:126–33. doi:10.1016/j.compstruct.2008.07.016.
- [6] Tabatabaei, S.A., Bedogni E, Melro AR, Ivanov DS, Lomov SV. Meso- FE simulation of progressive damage in textile composites using mesh superposition method. *ECCM17 - 17th Eur. Conf. Compos. Mater., Munich: 2016.*
- [7] Zhou Y, Lu Z, Yang Z. Progressive damage analysis and strength prediction of 2D plain weave composites. *Compos Part B Eng* 2013;47:220–9.
- [8] Lu Z, Zhou Y, Yang Z, Liu Q. Multi-scale finite element analysis of 2.5D woven fabric composites under on-axis and off-axis tension. *Comput Mater Sci* 2013;48:5–94.
- [9] Wan Y, Sun B, Gu B. Multi-scale structure modeling of damage behaviors of 3D orthogonal woven composite materials subject to quasi-static and high strain rate compressions. *Mech Mater* 2016;94:1–25. doi:10.1016/j.mechmat.2015.11.012.
- [10] Fang G, Liang J, Lu Q, Wang B, Wang Y. Investigation on the compressive properties of the three dimensional four-directional braided composites. *Compos Struct* 2011;93:392–405. doi:10.1016/j.compstruct.2010.09.002.
- [11] Zhang D, Waas AM, Yen CF. Progressive damage and failure response of hybrid 3D textile composites subjected to flexural loading, part II: Mechanics based multiscale computational modeling of progressive damage and failure. *Int J Solids Struct* 2015;75–76:321–35. doi:10.1016/j.ijsolstr.2015.06.033.
- [12] Elias A, Laurin F, Kaminski M, Gornet L. Experimental and numerical investigations of low energy/velocity impact damage generated in 3D woven composite with polymer matrix. *Compos Struct* 2017;159:228–39. doi:10.1016/j.compstruct.2016.09.077.
- [13] Lapczyk I, Hurtado J a. Progressive damage modeling in fiber-reinforced materials. *Compos Part A Appl Sci Manuf* 2007;38:2333–41. doi:10.1016/j.compositesa.2007.01.017.
- [14] Lomov S V., Ivanov D, Verpoest I, Zako M, Kurashiki T, NAKAI H, et al. Meso-FE modelling of textile composites: Road map, data flow and algorithms. *Compos Sci Technol* 2007;67:1870–91. doi:10.1016/j.compscitech.2006.10.017.
- [15] Zako M, Uetsuji Y, Kurashiki T. Finite element analysis of damaged woven fabric composite materials. *Compos Part B Eng* 2003;507–16.
- [16] Kachanov L. Time of the rupture process under creep conditions. *Isv Akad Nauk SSR* 1958;8:26–31.
- [17] Green SD, Matveev MY, Long AC, Ivanov D, Hallett SR. Mechanical modelling of 3D woven composites considering realistic unit cell geometry. *Compos Struct* 2014;118:284–93.
- [18] Chen JF, Morozov EV, Shankar K. A combined elastoplastic damage model for progressive failure analysis of composite materials and structures. *Compos Struct* 2012;94:3478–89. doi:10.1016/j.compstruct.2012.04.021.
- [19] Vasiukov D, Panier S, Hachemi A. Non-linear material modeling of fiber-reinforced polymers based on coupled viscoelasticity–viscoplasticity with anisotropic continuous damage mechanics. *Compos Struct* 2015;132:527–35. doi:10.1016/j.compstruct.2015.05.027.
- [20] Isart N, Saïd B El, Ivanov DS, Hallett SR, Mayugo JA, Blanco N. Internal geometric modelling of 3D woven composites: A comparison between different approaches. *Compos Struct* 2015;132:1219–30. doi:10.1016/j.compstruct.2015.07.007.
- [21] Lapeyronnie P, Le Grogne P, Binétry C, Boussu F. Homogenization of the elastic behavior of a layer-to-layer angle-interlock composite. *Compos Struct* 2011;2795–807.
- [22] Nehme S, Hallal A, Fardoun F, Younes R, Hagege B, Aboura Z, et al. Numeric/analytical methods to evaluate the mechanical behavior of interlock composites. *J Compos Mater* 2011;45:1699–716.
- [23] Potter E, Pinho ST, Robinson P, Iannucci L, Mcmillan AJ. Mesh generation and geometrical modelling of 3D woven composites with variable tow cross-sections. *Comput Mater Sci* 2012;51:103–11. doi:10.1016/j.commatsci.2011.06.034.
- [24] Rahali Y, Goda I, Ganghoffer JF. Numerical identification of classical and nonclassical moduli of 3D woven textiles and analysis of scale effects. *Compos Struct* 2016;135:122–39. doi:10.1016/j.compstruct.2015.09.023.
- [25] Visrolia A, Meo M. Multiscale damage modelling of 3D weave composite by asymptotic homogenisation. *Compos Struct* 2013;95:105–13. doi:10.1016/j.compstruct.2012.07.018.
- [26] Wang XF, Wang XW, Zhou GM, Zhou CW. Multi-scale analyses of 3D woven composite base on periodicity boundary conditions. *J Compos Mater* 2007;41:1773–88.
- [27] Wendling A, Hivet G, Vidal-Sallé E, Boisse P. Consistent geometrical modelling of interlock fabrics. *Finite Elem Anal Des* 2014;93–105.
- [28] Lomov S, Perie G, Ivanov D, Verpoest I, Marsal D. Modeling three-dimensional fabrics and three-dimensional reinforced composites: challenges and solutions. *Text Res J* 2011;81:28–41. doi:10.1177/0040517510385169.
- [29] Lomov S V., Verpoest I, Cichosz J, Hahn C, Ivanov DS, Verleye B. Meso-level textile composites simulations: Open data exchange and scripting. *J Compos Mater* 2013;48:621–37. doi:10.1177/0021998313476327.
- [30] Naouar N, Vidal-Sallé E, Schneider J, Marie E, Boisse P. Meso-scale FE analyses of textile composite reinforcement deformation based on X-ray computed tomography. *Compos Struct* 2014:156–76.
- [31] Straumit I, Lomov S V., Wevers M. Quantification of the internal structure and automatic generation of voxel models of textile composites from X-ray computed tomography data. *Compos Part A Appl Sci Manuf* 2014;69:150–8. doi:10.1016/j.compositesa.2014.11.016.
- [32] Straumit I, Hahn C, Winterstein E, Plank B, Lomov S V., Wevers M. Computation of permeability of a non-crimp carbon textile reinforcement based on X-ray computed tomography images. *Compos Part A Appl Sci Manuf* 2016;81:289–95. doi:10.1016/j.compositesa.2015.11.025.
- [33] Aravand MA, Shishkina O, Straumit I, Liotta AH, Wicks SS, Wardle BL, et al. Internal geometry of woven composite laminates with “fuzzy” carbon nanotube grafted fibers. *Compos Part A Appl Sci Manuf* 2016;88:295–304. doi:10.1016/j.compositesa.2016.06.010.
- [34] Doitrand A, Fagian C, Irisarri FX, Hirsokorn M. Comparison between voxel and consistent meso-scale models of woven composites. *Compos Part A Appl Sci Manuf* 2015;73:143–54. doi:10.1016/j.compositesa.2015.02.022.
- [35] Kaddour AS, Hinton MJ. Input data for test cases used in benchmarking triaxial failure theories of composites. *J Compos Mater* 2012;46:2295–312. doi:10.1177/0021998312449886.
- [36] <http://www.rxsolutions.fr/> n.d.
- [37] Karahan M, Lomov S V., Bogdanovich AE, Mungalov D, Verpoest I. Internal geometry evaluation of non-crimp 3D orthogonal woven carbon fabric composite. *Compos Part A Appl Sci Manuf* 2010;41:1301–11. doi:10.1016/j.compositesa.2010.05.014.
- [38] Mühlstädt M, Seifert W, Maenz S, Jandt KD, Bossert J. Modeling of through-thickness intra-yarn volume fraction gradients in laminated woven fabrics. *ECCM17 - 17th Eur. Conf. Compos. Mater., Munich: 2016.*
- [39] Murakami S. Notion of Continuum Damage Mechanics and its Application to Anisotropic Creep Damage Theory. *J Eng Mater Technol* 1983;105:99–105. doi:10.1115/1.3225633.
- [40] Sidoroff F. Description of Anisotropic Damage Application to Elasticity. *Phys Non-Linearities Struct Anal* 1981:237–44. doi:10.1007/978-3-642-81582-9_35.
- [41] Bazant Z, Oh B. Crack band theory of concrete. *Mater Struct* 1983;16:155–77. doi:10.1007/BF02486267.

- [42] Qing H, Mishnaevsky Jr. L. 3D constitutive model of anisotropic damage for unidirectional ply based on physical failure mechanisms. *Comput Mater Sci* 2010;50:479–86.
- [43] Aha DW, Kibler D, Albert MK. Instance-Based Learning Algorithms. *Mach Learn* 1991;6:37–66. doi:10.1023/A:1022689900470.
- [44] Greggio N, Bernardino A, Laschi C, Dario P, Santos-Victor J. Fast estimation of Gaussian mixture models for image segmentation. *Mach Vis Appl* 2012;23:773–89. doi:10.1007/s00138-011-0320-5.
- [45] Chamis C. Mechanics of composite materials: Past, present and future. NASA Tech Memo 1984:1–40.